Applied Physics Letters ARTICLE pubs.aip.org/aip/apl

Velocity-field measurements in a GaN/AlN two-dimensional hole gas

Cite as: Appl. Phys. Lett. **127**, 032105 (2025); doi: 10.1063/5.0276423
Submitted: 17 April 2025 · Accepted: 5 July 2025 ·
Published Online: 22 July 2025

View Online Export Citation CrossMark

Joseph E. Dill,[1,a)] Jonah Shoemaker,[2] Kazuki Nomoto,[3] Jimy Encomendero,[3] Zexuan Zhang,[3] Chuan F. C. Chang,[4] Jie-Cheng Chen,[5] Feliciano Giustino,[6] Stephen Goodnick,[2] Debdeep Jena,[3,7,8] and Huili Grace Xing[3,7,8,a)]

AFFILIATIONS

[1]School of Applied and Engineering Physics, Cornell University, Ithaca, New York 14850, USA
[2]Department of Physics, Arizona State University, Tempe, Arizona 85281, USA
[3]School of Electrical and Computer Engineering, Cornell University, Ithaca, New York 14850, USA
[4]Department of Physics, Cornell University, Ithaca, New York 14850, USA
[5]Oden Institute for Computational Engineering and Sciences, The University of Texas at Austin, Austin, Texas 78712, USA
[6]Department of Physics, The University of Texas at Austin, Austin, Texas 78712, USA
[7]Department of Materials Science and Engineering, Cornell University, Ithaca, New York 14850, USA
[8]Kavli Institute at Cornell for Nanoscale Science, Cornell University, Ithaca, New York 14850, USA

[a)]**Authors to whom correspondence should be addressed:** jed296@cornell.edu and grace.xing@cornell.edu

ABSTRACT

We report measurements and an improved analysis methodology to characterize the velocity-field characteristics of a polarization-induced two-dimensional hole gas in a GaN/AlN heterostructure at both room and cryogenic temperatures, using pulsed voltage and current through a micrometer-scale constriction. These high-bias measurements are made possible by Ohmic contacts that remain sufficiently transparent ($<50\,\Omega$ mm above 10 mA/mm current) at cryogenic temperatures. We observe a room temperature saturation velocity of $(2.1 \pm 0.2) \times 10^6$ cm/s and associated mobility of ~7–12 cm^2/V s for a hole density of 4×10^{13} cm^{-2}, which increases to $(4.4 \pm 0.4) \times 10^6$ cm/s at 4.2 K, with an associated mobility of ~25–50 cm^2/V s. The measured ensemble hole saturation velocity in this geometry, which is suitable for field-effect transistor channels, is lower than that of holes measured in lightly-doped n-type 3D bulk GaN (6.63×10^6 cm/s), owing to the 2D geometry and high carrier density of the two-dimensional hole gas, and degraded hole mobility from recess etching. Measured velocity-field contours are corroborated against bulk density functional theory and two-dimensional full-band real-space cellular Monte Carlo simulations under different surface boundary conditions.

The success of GaN high electron mobility transistors (HEMTs) for high-frequency applications[1–3] has motivated the development of their p-channel counterpart for GaN integrated circuits.[4,5] These efforts have proven challenging, however, owing to the large heavy hole effective mass[6] ($m^*_{HH} \sim 2m_e$) and the large activation energy of Mg acceptor dopants in GaN[7–10] ($E_A = 135$–170 meV).

Polarization-induced doping in metal-polar[11,12] GaN/Al(Ga)N and nitrogen-polar[13] Al(Ga)N/GaN heterostructures has been developed as an alternative means of p-type doping, wherein polarization discontinuity and piezoelectric charge at the hetero-interface produce a two-dimensional hole gas (2DHG) confined to the GaN.[14] These p-GaN channels can be formed without intentional chemical dopants[10,13] and benefit from the lack of impurity scattering and high free carrier density, which boosts hole conductivity. As such, polarization-doped p-GaN channels have been the platform for the highest on-current stand-alone GaN p-channel field-effect transistors (pFETs)[15,16] and demonstrations of GaN CMOS circuits.[17–25]

The switching speed of CMOS circuits is set by the cutoff frequency of the constituent transistors, $2\pi f_T = 1/(L_g/v_s + \tau_{par})$, where L_g is the transistor gate length, v_s is the saturated ensemble carrier velocity, and τ_{par} is the time-delay from device parasitics. v_s sets an intrinsic limit on f_T, captured in Johnson's figure of merit,[26] JFOM $= v_s E_c/2\pi$, where E_c is the critical electric field.

The hole v_s in lightly-doped n-type 3D GaN has been measured by Ji *et al.*[27] in vertical p-i-n diode structures by optically exciting electron–hole pairs and measuring the resulting current through the

depleted region under ~ kV reverse bias. A v_s of 6.63×10^6 cm/s was reported at room temperature for a net donor doping density of 1.0×10^{16} cm^{-3}.

However, high-field vertical transport through a lightly doped bulk semiconductor is expected to differ from lateral transport of a high-density 2D carrier gas because the dimensional confinement and occupation of low-energy k-states by the large carrier density influence the scattering of high-energy carriers.[28] Switching speeds in GaN pFETs utilizing chemically doped channels have also been shown to be affected by field-induced acceptor ionization.[29] These conditions motivate a measurement of v_s in an undoped GaN/AlN 2DHG in this work.

v_s can be straightforwardly measured in an FET by RF time-delay-analysis[30–34] in which f_T is measured for transistors of varying L_g and fit to determine v_s. This measurement requires a FET with RF switching capability and a sufficiently low-leakage gate to perform an open de-embedding correction with the transistor channel pinched off.

In the absence of such a transistor, pulsed current–voltage ($I - V$) measurements of an etched constriction are a standard alternative means of electrically measuring v_s for lateral transport. This technique was first demonstrated in 1951 in Ge[35] and has since been reported in various bulk semiconductors,[36–39] 2DEGs,[40–44] and 2D materials.[45] High-field conductivity measurements in linear transfer length method (L-TLM) and field-effect transistor structures with no constriction have also been reported.[46–50]

For this technique, a pulsed voltage V_a is applied, and the current I is measured between Ohmic contacts on either side of an etched constriction of width w and length ℓ [see Figs. 1(b), 1(g), and 1(h)]. If the carrier density n_{2d} is known (e.g., from Hall effect measurement), the ensemble drift velocity v_d can be deduced by

$$v_d = \frac{I}{q n_{2d} w}, \tag{1}$$

with the corresponding electric field inside the constriction given by

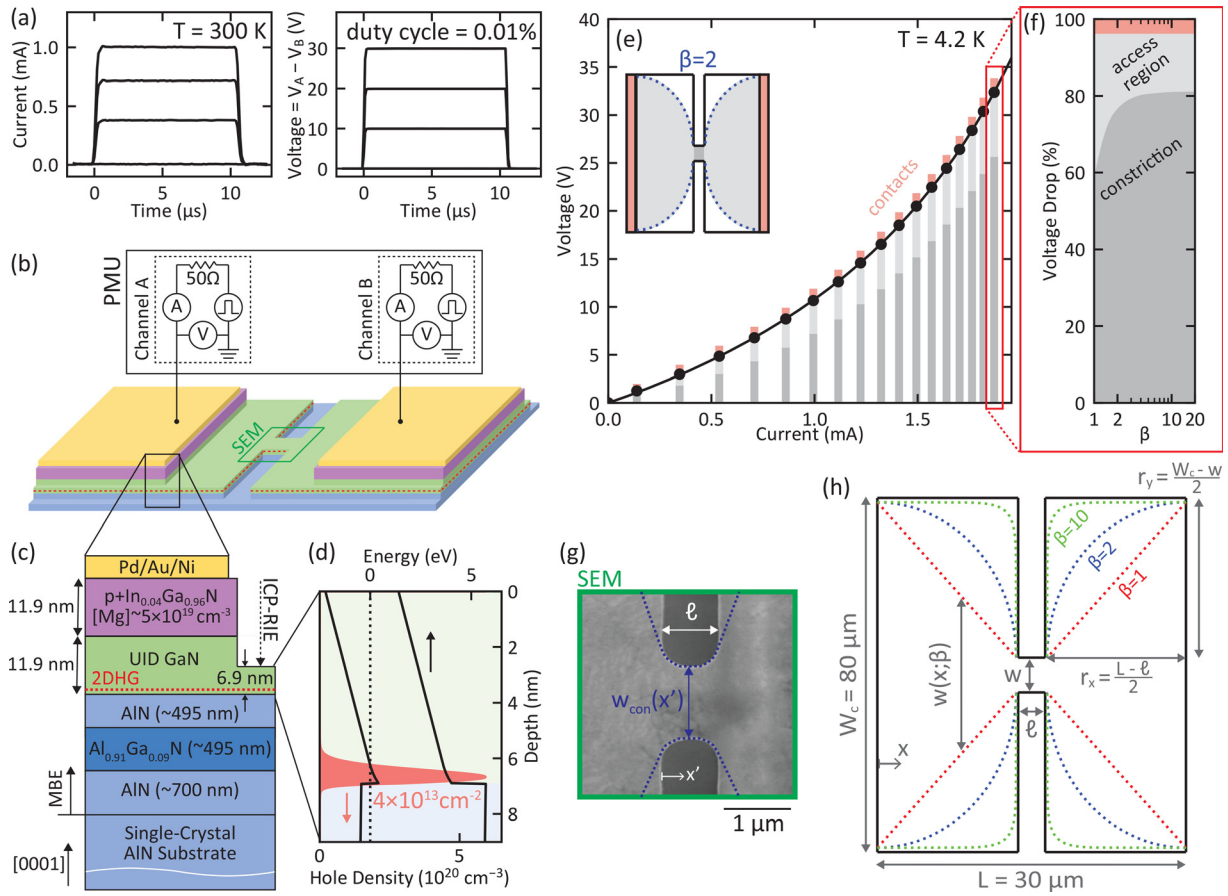

FIG. 1. (a) Measured current (left) and voltage (right) waveforms at room temperature for four voltage pulses from 0 to 30 V. (b) Circuit diagram of the pulsed measurement unit (PMU) and constriction test structure (not to scale) in a two-point $I - V$ configuration. (c) Device heterostructure. (d) Energy band diagram and 2DHG formation at the GaN/AlN interface. (e) Measured voltage vs current at T = 4.2 K, subdivided into the inferred voltage drops in the constriction (dark grey), the access regions (light grey), and the contacts (red). (Inset) Top-view of constriction test structure (not to scale), assuming an elliptical current profile in the access regions ($\beta = 2$). (f) Percentage of applied voltage dropped in the contacts, access regions, and constriction for the highest-voltage measurement in (e) as a function of the curvature parameter β defining the current-confinement profile in the access regions. (g) SEM image of an etched constriction. (h) Constriction test structure diagram with labeled dimensions and variables. Three exemplary current-confinement profiles are plotted [mathematical expression provided in Eq. (11)]: $\beta = 1$ (trapezoidal, red), $\beta = 2$ (elliptical, blue), and $\beta = 10$ (nearly rectangular, green).

$$E = \frac{V_a - V_{parasitic}}{l}, \tag{2}$$

where $V_{parasitic}$ accounts for any voltage loss between the constriction and the $I-V$ probes. Measured velocity-field curves are commonly fit with the empirical Caughey-Thomas relation,[51,52]

$$v(E) = \frac{\mu E}{\left(1 + \left(\frac{\mu E}{v_s}\right)^{\alpha}\right)^{1/\alpha}}, \tag{3}$$

to extract v_s and the low-field mobility μ, with $\alpha \sim 1$ as a phenomenological fitting parameter.

The device heterostructure utilized in this study [see Fig. 1(c)] was grown by molecular beam epitaxy on a single-crystal AlN substrate.[53] The AlN substrate surface was cleaned before growth by Al-flux polishing,[54] then a 1.7 μm buffer layer was grown, consisting of two unintentionally doped (UID) AlN layers above and below a ~495 nm thick UID $Al_{0.91}Ga_{0.09}N$ layer. This intermediate AlGaN layer serves to getter donor Si impurities within the buffer layer and prevent hole compensation in the subsequently-grown epitaxial layers.[55] An 11.9 nm layer of UID GaN was grown above the AlN buffer. Polarization discontinuity at this GaN/AlN interface and strain-induced piezoelectric charge produce a 2DHG in the GaN[10] [see energy band diagram in Fig. 1(d)]. Finally, an 11.9 nm p+$In_{0.04}Ga_{0.96}N$ capping layer was grown to facilitate Ohmic contact to the 2DHG.[15,16] Downward diffusion of Mg from the p+InGaN layer into the UID GaN layer is expected to be negligible.[56] Additional details of the epitaxy are discussed in Refs. 6 and 53.

Unannealed Pd/Au/Ni Ohmic contacts were formed by electron beam evaporation and liftoff process, as discussed in previous works.[15,16] The large work function of Pd (~5.2 eV) as well as the reduced bandgap and activation energy of Mg dopants in the p+InGaN layer[57] all promote Ohmic contact to the underlying hole channel. The p+InGaN layer between the metal contacts was removed with a BCl_3 ICP-RIE recess etch, leaving a 6.9 nm GaN channel layer. A low RF plasma power of ~8 W was used to curb etch damage while maintaining a stable plasma; however, further improvements are necessary, as evidenced by the mobility degradation observed in this work. The constriction channels were patterned by optical lithography and isolated by ICP-RIE etching [see scanning electron microscopy (SEM) image in Fig. 1(g)].

Magnetotransport measurements of the recess-etched region showed a positive Hall coefficient from 4.2 to 300 K, confirming the presence of the 2DHG. The as-grown epitaxial sample had a sheet resistance of 5.9 kΩ/□ and a Hall mobility of 15 cm^2/V s. After recess etching, the sheet resistance increased to 16 kΩ/□, and the Hall mobility dropped to 10 cm^2/Vs. Nonetheless, we chose to study this p+InGaN-capped structure with a recess-etched channel over others with higher as-grown hole mobility[6,58] to maintain transparent hole contacts at low temperatures while accepting the trade-off that the hole mobility degrades under recess etching.

Self-consistent Poisson and 6-band $k \cdot p$ simulations[6,59] indicate that the Fermi level in the measured GaN/AlN structures lies ~40 meV below the heavy hole (HH) Γ-point, and ~30 meV below the light hole (LH) Γ-point, such that carriers in both bands conduct in parallel. Reference 58 demonstrates that, in such cases, the longitudinal and transverse resistances are nonlinear with magnetic field, and low-field Hall effect measurements (~1 T) will underestimate the free carrier density. If the carrier mobilities are sufficiently large, this nonlinearity can be discerned from high-field (~10 T) magnetotransport measurements and fit with a four-parameter two-carrier classical Drude model to obtain the band-resolved densities. In Ref. 58, the LH and HH densities extracted in this manner agree well with the LH and HH densities obtained from Poisson-$k \cdot p$ simulation.

However, due to the degradation of hole mobility in the recess-etched regions of the measured sample, magnetotransport measurements did not yield sufficient non-linearity to constrain the four fitting parameters and extract the band-resolved densities. Thus, in the remainder of this Letter, $I-V$ measurements are primarily modeled in terms of current density J (with units A/mm) and conductivity σ. Estimates for the velocity $v = J/qn_{2d}$ and mobility $\mu = \sigma/qn_{2d}$ are obtained using the total (HH+LH) carrier density from Poisson-$k \cdot p$ modeling, $n_{k\cdot p} = 4.0 \times 10^{13}$ cm^{-2} [see Fig. 1(d)]. Material parameters for the $k \cdot p$ model were obtained from Ref. 60, and the surface Fermi level on the GaN surface was set 1.9 eV above the valence band.[61]

Two-point pulsed $I-V$ measurements of the constriction test structures were performed in a cryogenic probe station at temperatures from 4.2 to 400 K. As shown in Fig. 1(b), a Keithley 4200 Parameter Analyzer equipped with a two-channel pulsed measurement unit (PMU) was used to source a 10 μs pulsed voltage in channel A with channel B grounded while sampling the voltage and current waveforms in both channels [see Fig. 1(a)]. The PMU could produce a maximum voltage pulse of 40 V and a minimum pulse width of 0.8 μs. A duty cycle of 0.01% was used to minimize current-induced heating of the semiconductor channel from the high-voltage pulse. Voltage pulses of widths ranging from 1 to 100 μs produced comparable current output, indicating that such heating did not significantly influence the measured transport.

The voltage drops across the constriction, $V_{constriction}$, the contacts, $V_{contacts}$, and the intermediate "access regions," V_{access}, were subdivided from the total measured voltage, $V_a(I)$, as follows [see example in Figs. 1(e) and 1(f)]:

$$V_a(I) = \underbrace{V_{constriction}(I) + V_{access}(I)}_{V_{fitted}(I)} + \underbrace{2J_cR_c(J_c)}_{V_{contacts}(I)}. \tag{4}$$

Here, W_c is the width of the contact pad, $J_c = I/W_c$ is the current density through the contacts, and $R_c(J_c)$ is the total contact resistance of the nonlinear contacts [see Figs. 1(e) and 2] as a function of J_c. The sum of V_{access} (I) and $V_{contacts}$ (I) is equivalent to $V_{parasitic}$ in Eq. (2).

$R_c(J_c)$ was determined at each temperature from current-swept measurements of L-TLM structures on the same sample. The contacts exhibited nonlinear $I-V$, particularly below 200 K [see Fig. 2(a)], so a current-dependent L-TLM analysis was performed.

Treating the contacts as leaky back-to-back Schottky diodes, the voltage drop $V(J, d=0)$ across both contacts is expected to be repeatable but nonlinear in J_c. The total voltage drop between L-TLM pads with a finite spacing $d > 0$ is given by

$$V(J_c, d) = V(J_c, d=0) + J_cR_{sh}d, \tag{5}$$

where R_{sh} is the sheet resistance of the material between the pads. Dividing by J_c, we obtain a total resistance (in Ω mm) of

$$V(J_c, d)/J_c = \underbrace{V(J_c, d=0)/J}_{2R_c(J_c)} + R_{sh}d. \tag{6}$$

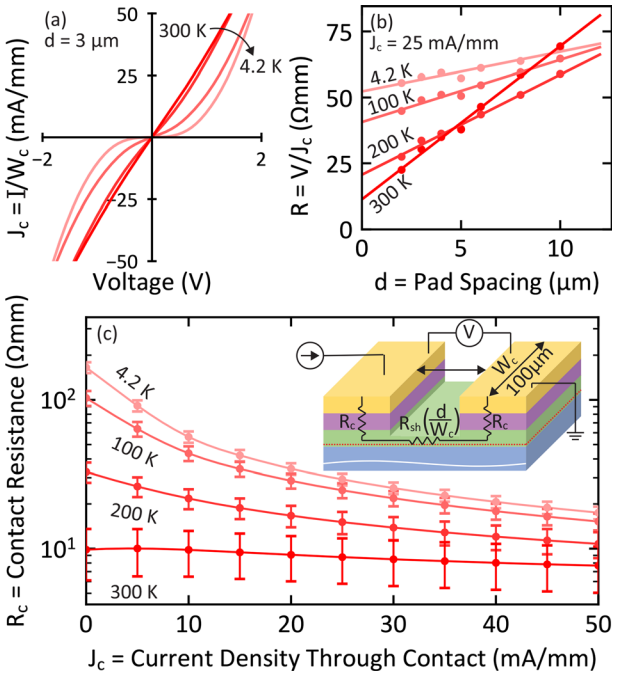

FIG. 2. Current-dependent contact resistance [red in Figs. 1(f) and 3(a)] analysis of linear transmission line method (L-TLM) measurements at four representative temperatures from 4.2 to 300 K. (a) $I-V$ curves from L-TLM pads with a spacing of $d = 3$ μm. (b) Total resistance (V/J_c) vs pad spacing d for a current density through the contact pad ($J_c = I/W_c$) of 25 mA/mm. $W_c = 100$ μm is the contact pad width. (c) Current density-dependent extraction of the contact resistance R_c. Points and error bars denote the average and standard deviation of measurements of multiple L-TLM test structure sets across the sample. (Inset) Device heterostructure and equivalent circuit diagram of the L-TLM measurement.

Using this equation, R_c was obtained at each sampled J_c from linear fits of the measured total resistance V/J_c vs pad spacing d [see example in Fig. 2(b)]. The measured $R_c(J_c)$ is plotted vs J_c in Fig. 2(c). Error bars in this figure denote the standard error of measurements from multiple L-TLM pad sets across the sample. At 300 K, the contact pads exhibited linear $I-V$ with $R_c \sim 10\,\Omega$ mm at all currents. At 4.2 K, the contacts became nonlinear, with a contact resistance ranging from $\sim$150–20 Ω mm between 0 and 50 mA/mm. Despite this diminished performance at cryogenic temperature, the contacts accounted for <5% of the total voltage drop across the measured constriction test structures [see Fig. 1(f)], validating that the current saturation observed in these structures is due to hole velocity saturation in the constriction rather than current choke in the contacts.

The voltage drop in the access regions of the test structure [$V_{\text{access}}(I)$ in Eq. (4)] is typically inferred[38,45] by assuming (1) that the electric fields in these regions are sufficiently below the saturation field $E_s = v_s/\mu$ that all transport is in the "mobility regime" ($v_d \approx \mu E$) with sheet resistance $R_{sh} = 1/qn\mu$ and (2) that the current between the contacts and the constriction flows within a trapezoidal profile [see red $\beta = 1$ contour in Fig. 1(h)]. Under these assumptions, the total voltage drop in the access regions is computed by

$$V_{\text{access}}(I) = 2\int_0^{r_x} IR_{sh}\frac{dx}{w(x)}, \tag{7}$$

where r_x is the distance between the contact and constriction and $w(x)$ is the width of the current-confinement profile at position x [see Fig. 1(h)].

In this investigation, however, both of these assumptions are modified. First, as seen in Eq. (4), rather than subtracting $V_{\text{access}}(I)$ to determine $V_{\text{constriction}}(I)$, we fit the entire voltage drop between the contact pads, $V_{\text{fitted}}(I)$. Doing so allows the hole velocity in the access regions to deviate from μE before the carriers enter the constriction and thus ensures that the inferred velocity-field curve and electric field distribution across the entire test structure are related self-consistently.

To do this, we first multiply Eq. (3) by qn_{2d}, which becomes

$$J(E) = \frac{\sigma E}{\left(1+\left(\frac{\sigma E}{J_s}\right)^{\alpha}\right)^{1/\alpha}}, \tag{8}$$

where $J_s = qn_{2d}v_s$ is the saturated current density. Solving Eq. (8) for E gives

$$E(J; E_s, J_s, \alpha) = E_s\left(\left(\frac{J_s}{J}\right)^{\alpha} - 1\right)^{-1/\alpha}, \tag{9}$$

with $E_s = v_s/\mu = J_s/\sigma$. Thus, the total voltage drop between $x = 0$ and $x = L$ [see Fig. 1(h)] when flowing a current I is given by

$$V(I; E_s, J_s, \alpha, \beta) = \int_0^L E\left(J = \frac{I}{w(x;\beta)}; E_s, J_s, \alpha\right)dx. \tag{10}$$

Additionally, rather than assuming a trapezoidal current-confinement profile in the access regions for $w(x)$, we use a super-elliptical equation as follows:

$$w(x;\beta) = \begin{cases} w_{con}(0) + 2r_y\left(1-\left(\frac{x}{r_x}\right)^{\beta}\right)^{1/\beta}, & x \le r_x, \\ w_{\text{con}}(x - r_x), & r_x < x \le r_x + \ell, \\ w_{\text{con}}(\ell) + 2r_y\left(1-\left(\frac{L-x}{r_x}\right)^{\beta}\right)^{1/\beta}, & x > r_x + \ell. \end{cases} \tag{11}$$

The curvature parameter β phenomenologically emulates varying degrees of current spreading in the access regions. A β value of 1 produces a trapezoidal profile, as used elsewhere.[38,45] However, this represents an upper-bound estimate for V_{access}. By varying β to larger values, we can also establish a lower-bound estimate for the inferred voltage drop in the access regions.

For the example data shown in Figs. 1(e) and 1(f), measured at 4.2 K, the access regions cumulatively account for between 38% and 15% of the total voltage drop when varying β from 1 to 20, respectively. We demonstrate later in this report that this choice of β has negligible impact on the measured value of v_s [see Fig. 4(b)] but does impact the inferred mobility and velocity-field curve [see Figs. 3(c) and 4(d)].

Example current-spread profiles for $\beta = 1$ (trapezoidal), $\beta = 2$ (elliptical), and $\beta = 10$ are plotted in Fig. 1(h), which also shows the coordinate system and variable definitions for Eq. (11). The $w_{\text{con}}(x')$ curve in Eq. (11) was determined graphically for each fabricated constriction from SEM micrographs [see example in Fig. 1(g)].

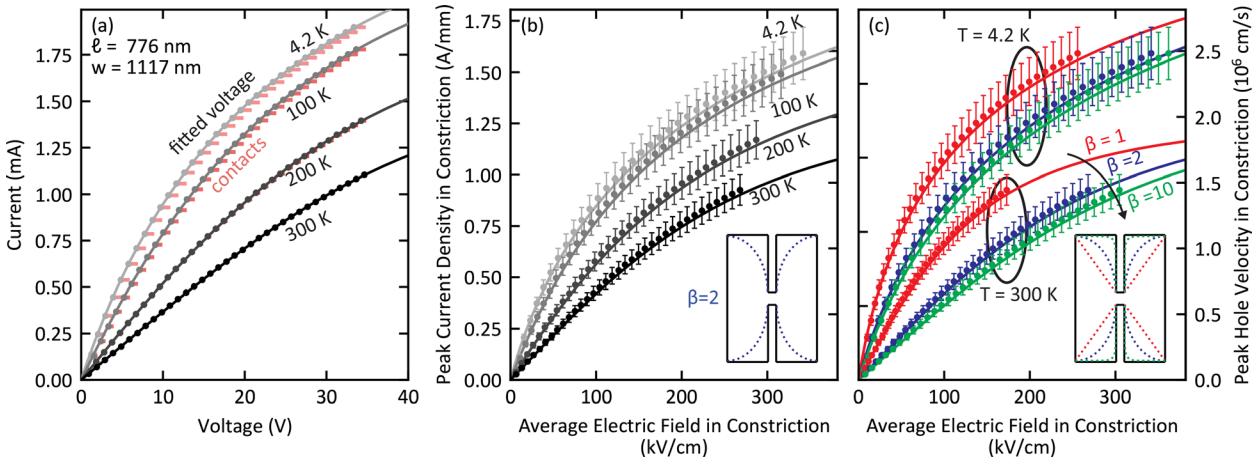

FIG. 3. (a) Measured current vs voltage curves (points) at select temperatures from 4.2 to 300 K for a constriction with $\ell = 776$ nm and $w_{min} = 1117$ nm, fit with Eq. (10) (solid line). Right-going red bars indicate the inferred voltage drop across the contacts, excluded from the fitted voltage [see Eq. (4)]. (b), (c) The corresponding current density/hole velocity (on the left/right axes, respectively) vs electric field curves from Eqs. (8)/(3) (solid line) plotted against the measured current density/hole velocity through the constriction at its narrowest point $I/min(w_{con}(x))$ and the average electric field $V_{constriction}/\ell$ in the constriction (symbols). Error bars reflect propagated uncertainty in the fit parameters in (a) and the measured constriction dimensions. The data in (b) assume an elliptical ($\beta = 2$) current-confinement profile in the access region. In (c), fits at T = 4.2 K and 300 K are compared for $\beta = 1$ (red), $\beta = 2$ (blue), and $\beta = 10$ (green). Insets in (b) and (c) show schematics of the respective current-confinement profiles [from Eq. (11)].

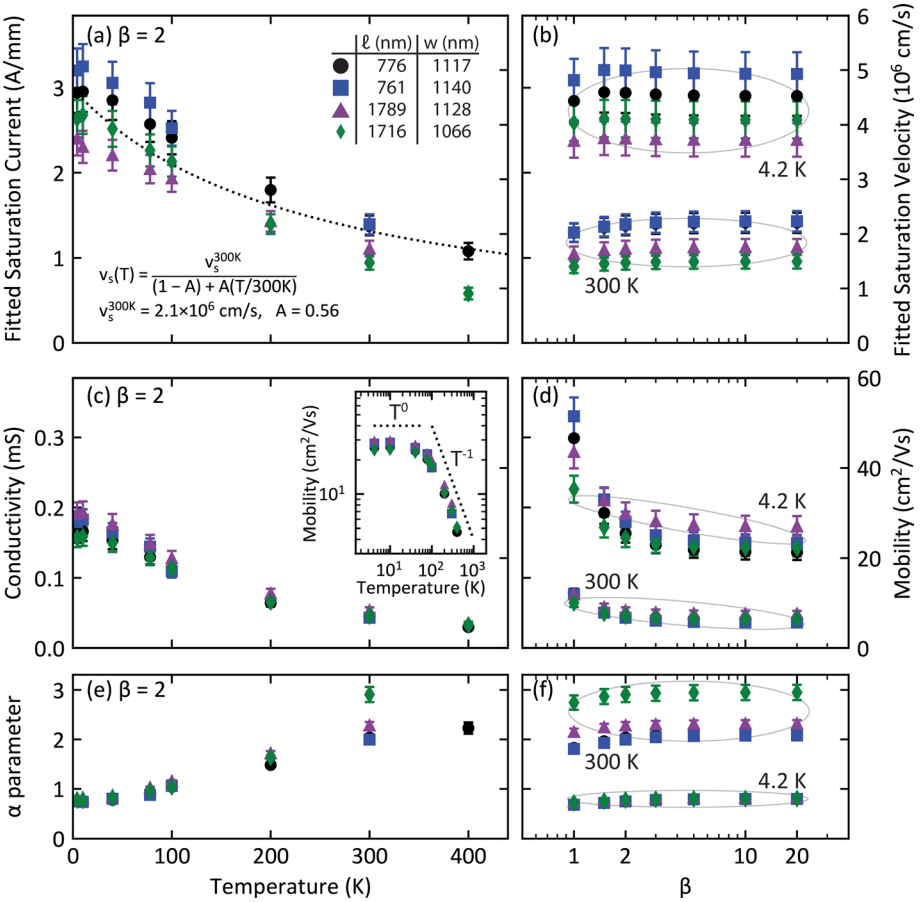

FIG. 4. Fit results/estimates (on the left/right axes) of (a), (b) saturation current/velocity, (c), (d) conductivity/mobility, and (e), (f) α parameter for four constriction test structures [dimensions given in inset to (a)]. (a), (c), (e) Fit results from 4.2 to 400 K, analyzed with $\beta = 2$. (b), (d), (f) Fit results at 4.2 and 300 K, analyzed with β ranging from 1 to 20. (a) Assuming a temperature-independent 2DHG concentration,[58] the temperature-dependent v_s from all measured constrictions are well-fit by an empirical model,[62] with $v_s(300\,K) = 2.1 \times 10^6$ cm/s. (inset to c) The temperature-dependent mobilities follow T^{-1} and T^0 power laws above and below ~ 50 K. Note: plotted J_s and v_s in (a), (b) denote an asymptotic fit parameter in the Caughey-Thomas model[51] [Eq. (3)] and are larger than any measured current density or velocity. These results demonstrate that the v_s value inferred from constriction velocity-field measurements is robust against the assumed current-spreading model.

Measured V_{fitted} vs I curves were fit numerically to Eq. (10) with E_s, J_s, and α as free parameters and with a particular choice of β. Example model fits assuming an elliptical current-spread profile ($\beta = 2$) are plotted in Fig. 3(a) at select temperatures from 4.2 to 300 K. The corresponding best-fit parameters are plotted in Figs. 4(a), 4(c), and 4(e) for four unique constriction test structures at temperatures from 4.2 to 400 K. σ and J_s are indicated on the left axes of Figs. 4(a) and 4(c), respectively, with the corresponding estimates of μ and v_s (from division by $qn_{k\cdot p}$) indicated on the right axes of Figs. 4(b) and 4(d), respectively.

Roughly 20% variation in σ is observed between the four measured test structures. This variation likely arises from non-uniformity of defect density or thickness in the epitaxial GaN or non-uniformity in the recess etch depth or etch-induced damage.

Consistent with previous reports of GaN/AlN 2DHG transport,[10,53,55,58] the inferred mobilities decrease with a T^{-1} power law above ~ 50 K and saturate at lower temperatures (T^0 power law) at $\sim 25\ cm^2/Vs$ [see inset to Fig. 4(c)]. Previous simulations of hole mobility in GaN/AlN 2DHGs have found acoustic phonons to be the dominant scattering mechanism.[59] Analytical models for acoustic deformation potential mobility in two-dimensional systems go as[63] $\mu_{2d}^{ADP} \sim (2k_B T)^{-1}$, so the observed power law behavior is expected.

The observed saturation velocities in Fig. 4(a) decrease from $\sim 4.4 \times 10^6$ cm/s at 4.2 K to $\sim 1.5 \times 10^6$ cm/s at 400 K. The saturation velocities are well-fit by the phenomenological fitting equation,[62]

$$v_s(T) = \frac{v_s(300\,\mathrm{K})}{(1-A) + A\left(\frac{T}{300\,\mathrm{K}}\right)}, \tag{12}$$

with $v_s(300\,\mathrm{K}) = 2.1 \times 10^6$ cm/s and $A = 0.56$.

The room temperature lateral v_s in these 2DHG structures, where the hole Fermi level is $\sim$40 meV below the top of the valence band, is $\sim 3\times$ lower than that measured for vertical transport in lightly doped 3D n-type GaN[27] (6.63×10^6 cm/s), where the hole quasi-Fermi level generated by photon absorption lies above the valence band. Previous room temperature constriction measurements of AlGaN/GaN HEMTs[41] showed a $\sim 10\times$ higher lateral v_s of $\sim 3 \times 10^7$ cm/s for a free electron concentration of $2 \times 10^{13}\ cm^{-2}$ and mobility of $430\ cm^2/Vs$.

To assess the influence that the assumed current spreading in the access regions had on the extracted transport parameters, multiple model fits were performed for all measured constriction test structures and at all temperatures, varying β from 1 to 20. Figure 3(c) shows the peak current density and hole velocity in the constriction at 4.2 and 300 K for β values of 1, 2, and 10. The corresponding fit parameters for all four test structures are plotted in Figs. 4(b), 4(d), and 4(f).

As is expected, the extracted conductivity/mobility values are strongly influenced by the choice of β, decreasing by $\sim 2\times$ between $\beta = 1$ and $\beta = 5$ (above which the fit results are unchanged). However, the extracted values of v_s (as well as α) vary by only $\sim$5% between $\beta = 1$ and $\beta = 20$, which is within the error bar from all other sources of uncertainty in the measurement. This consistency is also seen in Fig. 3(c), in which the 300 K velocity-field curves for $\beta = 1$, 2, and 10 extrapolate to a similar saturation velocity, despite variation in the inferred low-field velocities. These results demonstrate that the v_s value inferred from constriction velocity-field measurements is robust against the assumed current-spreading model.

High electric field transport of holes in a GaN 2DHG was also investigated by a two-dimensional full-band real-space cellular Monte Carlo simulation.[64] These simulations emulated the constriction measurement by quantifying the total hole flux through cross sections near both contacts and dividing by the local hole concentration. The details of these simulations are discussed in the supplementary material. The resulting velocity-field curves, simulated at 300 K, are plotted in Fig. 5, along with the bulk transport result from density functional theory (DFT) and two measured contours at 300 K from Fig. 3(b).

The simulated real-space device consisted of a 6.9 nm GaN thin film on an AlN substrate with length ℓ in the current flow direction [see inset to Fig. 5(a)]. Simulations were performed under two boundary conditions. (1) the "free surface E_F" condition—where the GaN surface potential was calculated to maintain zero electric field at the surface in a Neumann boundary condition, i.e., flatband GaN perpendicular to the GaN/AlN interface, and (2) the "pinned surface E_F"

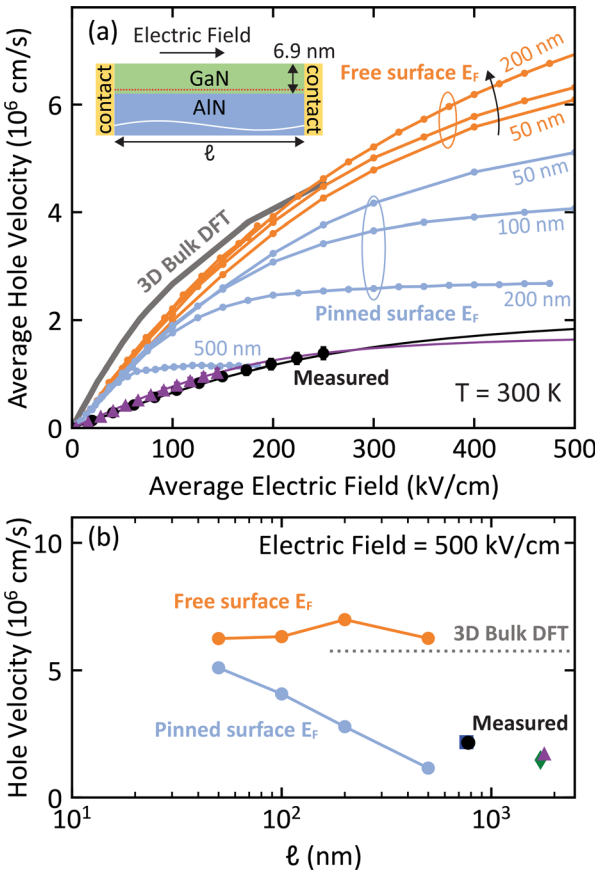

FIG. 5. (a) Average hole velocity vs electric field curves at 300 K from three-dimensional bulk DFT simulation (grey line), and two-dimensional full-band real-space cellular Monte Carlo simulation (blue/orange points with lines), and constriction measurements [points—color convention given in Fig. 4(a)]. The real-space simulations modeled a 6.9 nm GaN/AlN substrate heterostructure of length ℓ (top left inset) with the surface electric field set to zero (orange) and with the GaN surface Fermi level pinned to 1.9 eV above the valence band[61] (light blue) for ℓ from 50 to 500 nm. (b) Measured and simulated hole velocities at an electric field of 500 kV/cm [from fitting to Eq. (3)] as a function of channel length.

condition—where the GaN surface potential was fixed at all points with the Fermi level 1.9 eV above the valence band[61] in a Dirichlet boundary condition. The simulated low-field hole velocities give a mobility of $\sim 20\,\mathrm{cm}^2/\mathrm{Vs}$ at room temperature, in good agreement with previous simulations.[59] The measured room temperature mobility in the constrictions was 7–12 $\mathrm{cm}^2/\mathrm{Vs}$, depending on the choice of β [see Fig. 4(d)]. The device simulation only accounted for phonon scattering, so the measured mobility is expected to be lower due to extrinsic scattering, likely at point defects in the epitaxial structure or material defects introduced during recess etching of the p+InGaN layer [see Fig. 1(b)]. For reference, the measured low-temperature (<100 K) hole mobility in these fabricated constrictions is $\sim 10\times$ lower than that of the heavy hole and $\sim 400\times$ lower than that of the light hole in similar to-grown UID GaN/AlN structures.[6,58]

The bulk DFT simulation (grey line in Fig. 5) gives a room temperature hole mobility of 36 $\mathrm{cm}^2/\mathrm{Vs}$. This result is slightly lower than the in-plane hole mobility of 46 $\mathrm{cm}^2/\mathrm{Vs}$ simulated by Leveillee *et al.*,[65] which accounted for the many-body GW correction to the quasiparticle eigenvalues. This correction has the effect of increasing band curvature and, consequently, mobility. The hole velocities from bulk DFT extrapolate [by Eq. (3)] to a saturation velocity of 7.3×10^6 cm/s, slightly above that previously measured for holes in lightly doped n-type 3D bulk GaN[27] (6.63×10^6 cm/s). As seen in Fig. 5(a), the free surface condition in the real-space 2DHG structure produced similar velocity-field curves to the bulk simulation, regardless of device size.

However, the pinned Fermi level case resulted in a harder velocity plateau due to pinch-off effects. Consistent with the long-channel mobility model of a field-effect transistor, the pinned surface potential acts as a gate, and the saturation current increases with decreasing ℓ. The hole velocities at an electric field of 500 kV/cm [by Eq. (3)] for the bulk DFT simulation and the real-space simulations are plotted as a function of ℓ in Fig. 5(b). Hole velocities from the constriction measurements are also plotted vs constriction length, showing a similar increase with decreasing transport distance. In the pinned surface E_F case, the simulated velocity-field contour for $\ell = 500$ nm plateaus at a saturation velocity of 1.2×10^6 cm/s, while the measured constriction with $\ell = 776$ nm exhibited a saturation velocity of $(2.2\pm0.2)\times10^6$ cm/s. Shrinking the simulated structure to $\ell = 50$ nm, the velocity field approaches that of the bulk and free surface conditions. Thus, the simulated Fermi level pinning represents a limiting case of the surface potential, resulting in a more drastic pinch-off than is present in the measured devices. Nonetheless, the trend observed in the measured and simulated high-field hole velocities suggests that gate length scaling is a viable means of boosting saturated hole currents in p-channel GaN FETs.

In conclusion, the velocity-field characteristics of a GaN/AlN 2DHG have been measured between 4.2 and 400 K by pulsed electrical measurements of etched constriction test structures. The analysis procedure that we have presented improves upon previous reports of this method by accounting for varying levels of current spreading and ensuring consistency between the inferred mobility in the access and constriction regions of the test structure.

Assuming a temperature-independent hole density[58] of 4.0×10^{13} cm^{-2} from Poisson-$k\cdot p$ simulations, a saturation velocity of 2.1×10^6 cm/s is inferred at 300 K, increasing to 4.4×10^6 cm/s at 4.2 K. The inferred value of v_s is shown to be unaffected by the assumed current-spread profile in the access regions between the contacts and constriction. The measured velocities are corroborated against real-space full-band Monte Carlo simulations of GaN/AlN heterostructures with varying lengths. The simulated hole velocities depend significantly on surface Fermi level pinning. This study suggests that gate length scaling is a viable means of boosting saturation current in GaN pFETs. Future constriction experiments would benefit from improved Ohmic contacts;[15,16] reduced pad-to-constriction spacing; higher as-grown hole mobility[6,58] or enhanced mobility from strain engineering;[59,66] surface passivation to regulate the surface Fermi level condition; and a systematically varied 2DHG concentration, either by gating[48–50] or by successive recess etching of the GaN channel layer,[40] but without degrading the GaN surface quality[67] or hole mobility.

See the supplementary material for a discussion on the technical details of the Monte Carlo simulations presented in Fig. 5.

This work was supported in part by ULTRA, an Energy Frontier Research Center funded by the U.S. Department of Energy (DOE), Office of Science, Basic Energy Sciences (BES) (Award No. DE-SC0021230) (Monte Carlo simulation), and by SUPREME, one of seven centers in JUMP 2.0, a Semiconductor Research Corporation (SRC) program sponsored by DARPA (electrical measurements and analysis). The authors at Cornell University acknowledge financial support from Asahi Kasei (substrates) and AFOSR (Grant No. FA9550-20-1-0148) (device fabrication). This work made use of the Cornell Center for Materials Research Shared Facilities (Hall characterization). This work was performed in part at the Cornell NanoScale Facility, a member of the National Nanotechnology Coordinated Infrastructure (NNCI), which is supported by the National Science Foundation (Grant No. NNCI-2025233). The authors benefited from discussions of these results with Professor James Hwang, Dr. Samuel James Bader, and Dr. Reet Chaudhuri.

AUTHOR DECLARATIONS

Conflict of Interest

The authors have no conflicts to disclose.

Author Contributions

Joseph E. Dill: Conceptualization (supporting); Data curation (lead); Formal analysis (lead); Investigation (lead); Methodology (lead); Visualization (lead); Writing – original draft (lead). **Jonah Shoemaker:** Data curation (supporting); Investigation (supporting); Software (lead); Writing – original draft (supporting). **Kazuki Nomoto:** Methodology (supporting); Resources (equal). **Jimy Encomendero:** Data curation (supporting); Methodology (supporting). **Zexuan Zhang:** Resources (equal). **Chuan F. C. Chang:** Data curation (supporting); Formal analysis (supporting); Investigation (supporting); Writing – review & editing (supporting). **Jie-Cheng Chen:** Methodology (supporting); Software (supporting). **Feliciano Giustino:** Supervision (supporting). **Stephen Goodnick:** Supervision (supporting). **Debdeep Jena:** Funding acquisition (equal); Supervision (supporting); Writing – review & editing (supporting). **Huili Grace Xing:** Conceptualization (lead); Funding acquisition (equal); Supervision (lead); Writing – review & editing (lead).

DATA AVAILABILITY

The data that support the findings of this study are available from the corresponding authors upon reasonable request.

REFERENCES

[1]K. Hoo Teo, Y. Zhang, N. Chowdhury, S. Rakheja, R. Ma, Q. Xie, E. Yagyu, K. Yamanaka, K. Li, and T. Palacios, J. Appl. Phys. **130**, 160902 (2021).
[2]J. Würfl, T. Palacios, H. G. Xing, Y. Hao, and M. Schubert, Appl. Phys. Lett. **125**, 070401 (2024).
[3]H. Amano, Y. Baines, E. Beam, M. Borga, T. Bouchet, P. R. Chalker, M. Charles, K. J. Chen, N. Chowdhury, R. Chu, C. De Santi, M. M. De Souza, S. Decoutere, L. Di Cioccio, B. Eckardt, T. Egawa, P. Fay, J. J. Freedsman, L. Guido, O. Häberlen, G. Haynes, T. Heckel, D. Hemakumara, P. Houston, J. Hu, M. Hua, Q. Huang, A. Huang, S. Jiang, H. Kawai, D. Kinzer, M. Kuball, A. Kumar, K. B. Lee, X. Li, D. Marcon, M. März, R. McCarthy, G. Meneghesso, M. Meneghini, E. Morvan, A. Nakajima, E. M. S. Narayanan, S. Oliver, T. Palacios, D. Piedra, M. Plissonnier, R. Reddy, M. Sun, I. Thayne, A. Torres, N. Trivellin, V. Unni, M. J. Uren, M. Van Hove, D. J. Wallis, J. Wang, J. Xie, S. Yagi, S. Yang, C. Youtsey, R. Yu, E. Zanoni, S. Zeltner, and Y. Zhang, J. Phys. D. Appl. Phys. **51**, 163001 (2018).
[4]S. J. Bader, H. Lee, R. Chaudhuri, S. Huang, A. Hickman, A. Molnar, H. G. Xing, D. Jena, H. W. Then, N. Chowdhury, and T. Palacios, IEEE Trans. Electron Devices **67**, 4010–4020 (2020).
[5]J. Wei, Z. Zheng, G. Tang, H. Xu, G. Lyu, L. Zhang, J. Chen, M. Hua, S. Feng, T. Chen, and K. J. Chen, IEEE Trans. Electron Devices **71**, 1365–1382 (2024).
[6]C. F. Chang, J. E. Dill, Z. Zhang, J.-C. Chen, N. Pieczulewski, S. J. Bader, O. A. Valenzuela, S. A. Crooker, F. F. Balakirev, R. D. McDonald *et al.*, arXiv:2501.16213 (2025).
[7]W. Kim, A. Salvador, A. E. Botchkarev, O. Aktas, S. N. Mohammad, and H. Morcoç, Appl. Phys. Lett. **69**, 559–561 (1996).
[8]W. Götz, N. M. Johnson, J. Walker, D. P. Bour, and R. A. Street, Appl. Phys. Lett. **68**, 667–669 (1996).
[9]D. J. Kim, D. Y. Ryu, N. A. Bojarczuk, J. Karasinski, S. Guha, S. H. Lee, and J. H. Lee, J. Appl. Phys. **88**, 2564–2569 (2000).
[10]R. Chaudhuri, S. J. Bader, Z. Chen, D. A. Muller, H. G. Xing, and D. Jena, Science **365**, 1454–1457 (2019).
[11]M. S. Shur, A. D. Bykhovski, R. Gaska, J. W. Yang, G. Simin, and M. A. Khan, Appl. Phys. Lett. **76**, 3061–3063 (2000).
[12]G. Li, D. Jena, R. Wang, B. Song, J. Verma, Y. Cao, S. Ganguly, A. Verma, J. Guo, and H. G. Xing, IEEE Electron Device Lett. **34**, 852–854 (2013).
[13]C. Yu, Z. Zhang, D. Jena, H. G. Xing, and Y. Cho, Appl. Phys. Lett. **125**, 232101 (2024).
[14]O. Ambacher, J. Smart, J. R. Shealy, N. G. Weimann, K. Chu, M. Murphy, W. J. Schaff, L. F. Eastman, R. Dimitrov, L. Wittmer, M. Stutzmann, W. Rieger, and J. Hilsenbeck, J. Appl. Phys. **85**, 3222–3233 (1999).
[15]K. Nomoto, R. Chaudhuri, S. J. Bader, L. Li, A. Hickman, S. Huang, H. Lee, T. Maeda, H. W. Then, M. Radosavljevic, P. Fischer, A. Molnar, J. C. M. Hwang, H. G. Xing, and D. Jena, in *2020 IEEE International Electron Devices Meeting* (IEEE, 2020), Vol. 2020, pp. 8.3.1–8.3.4.
[16]S. J. Bader, R. Chaudhuri, A. Hickman, K. Nomoto, S. Bharadwaj, H. W. Then, H. G. Xing, and D. Jena, in *2019 IEEE Int. Electron Devices Meeting* (IEEE, 2019), pp. 4.5.1–4.5.4.
[17]H. Hahn, B. Reuters, S. Kotzea, G. Lükens, S. Geipel, H. Kalisch, and A. Vescan, in *72nd Device Research Conference* (IEEE, 2014), pp. 259–260.
[18]R. Chu, Y. Cao, M. Chen, R. Li, and D. Zehnder, IEEE Electron Device Lett. **37**, 269–271 (2016).
[19]A. Nakajima, S. Kubota, K. Tsutsui, K. Kakushima, H. Wakabayashi, H. Iwai, S.-I. Nishizawa, and H. Ohashi, IET Power Electron. **11**, 689–694 (2018).
[20]N. Chowdhury, Q. Xie, M. Yuan, K. Cheng, H. W. Then, and T. Palacios, IEEE Electron Device Lett. **41**, 820–823 (2020).
[21]Z. Zheng, L. Zhang, W. Song, S. Feng, H. Xu, J. Sun, S. Yang, T. Chen, J. Wei, and K. J. Chen, Nat. Electron. **4**, 595–603 (2021).
[22]Q. Xie, M. Yuan, J. Niroula, J. A. Greer, N. S. Rajput, N. Chowdhury, and T. Palacios, in *2022 International Electron Devices Meeting* (IEEE, 2022), Vol. 2022, pp. 35.3.1–35.3.4.
[23]T. Li, J. Wei, M. Zhang, J. Yu, Y. Lao, S. Liu, M. Zhong, J. Cui, J. Yang, H. Yang *et al.*, in *2024 IEEE International Electron Devices Meeting (IEDM)* (IEEE, 2024), pp. 1–4.
[24]H. Qi, T. Li, J. Yu, J. Cui, J. Yang, S. Liu, Y. Lao, H. Yang, X. Yang, M. Wang, B. Shen, Y. Zhang, S. Feng, M. Zhang, and J. Wei, IEEE Trans. Electron Devices **72**, 1663–1668 (2025).
[25]T. Li, J. Yu, S. Liu, Y. Lao, J. Cui, H. Qi, J. Yang, H. Yang, X. Yang, M. Wang *et al.*, in *IEEE Transactions on Electron Devices* (IEEE, 2025).
[26]E. Johnson, in *IRE International Convention Record* (Institute of Electrical and Electronics Engineers, 1966), Vol. 13, pp. 27–34.
[27]D. Ji, B. Ercan, and S. Chowdhury, IEEE Electron Device Lett. **41**, 23–25 (2020).
[28]T. Fang, R. Wang, G. Li, H. Xing, S. Rajan, and D. Jena, IEEE Electron Device Lett. **33**, 709–711 (2012).
[29]N. Chowdhury, Q. Xie, J. Niroula, N. S. Rajput, K. Cheng, H. W. Then, and T. Palacios, in *2020 IEEE International Electron Devices Meeting (IEDM)* (IEEE, 2020), p. 5.
[30]T. Suemitsu, ECS Trans. **16**, 65 (2008).
[31]T. Suemitsu, K. Shiojima, T. Makimura, and N. Shigekawa, Jpn. J. Appl. Phys. **44**, L211 (2005).
[32]T. Palacios, A. Chakraborty, S. Keller, U. K. Mishra *et al.*, IEEE Electron Device Lett. **27**, 877–880 (2006).
[33]B. Sensale-Rodriguez, J. Guo, R. Wang, J. Verma, G. Li, T. Fang, E. Beam, A. Ketterson, M. Schuette, P. Saunier *et al.*, Solid-State Electron. **80**, 67–71 (2013).
[34]B. Romanczyk, M. Guidry, X. Zheng, H. Li, E. Ahmadi, S. Keller, and U. K. Mishra, IEEE Trans. Electron Devices **67**, 1542–1546 (2020).
[35]E. J. Ryder and W. Shockley, Phys. Rev. **81**, 139–140 (1951).
[36]W. V. Muench and E. Pettenpaul, J. Appl. Phys. **48**, 4823–4825 (1977).
[37]J. M. Barker, D. K. Ferry, D. D. Koleske, and R. J. Shul, J. Appl. Phys. **97**, 063705 (2005).
[38]I. Khan and J. Cooper, IEEE Trans. Electron Devices **47**, 269–273 (2000).
[39]J. Barker, R. Akis, T. Thornton, D. Ferry, and S. Goodnick, Phys. Status Solidi **190**, 263–270 (2002).
[40]S. Bajaj, O. F. Shoron, P. S. Park, S. Krishnamoorthy, F. Akyol, T.-H. Hung, S. Reza, E. M. Chumbes, J. Khurgin, and S. Rajan, Appl. Phys. Lett. **107**, 1–5 (2015).
[41]J. M. Barker, D. K. Ferry, S. M. Goodnick, D. D. Koleske, A. Allerman, and R. J. Shul, J. Vac. Sci. Technol. B **22**, 2045–2050 (2004).
[42]Y. Zhang, Z. Xia, J. Mcglone, W. Sun, C. Joishi, A. R. Arehart, S. A. Ringel, and S. Rajan, IEEE Trans. Electron Devices **66**, 1574–1578 (2019).
[43]B. A. Danilchenko, N. A. Tripachko, A. E. Belyaev, S. A. Vitusevich, H. Hardtdegen, and H. Lüth, Appl. Phys. Lett. **104**, 072105 (2014).
[44]Z. Xia, "Materials and device engineering for high performance β-Ga_2O_3-based electronics dissertation," Ph.D. thesis (The Ohio State University, 2020).
[45]M. Winters, J. Hassan, H. Zirath, E. Janzén, and N. Rorsman, J. Appl. Phys. **113**, 193708 (2013).
[46]L. Ardaravičius, A. Matulionis, J. Liberis, O. Kiprijanovic, M. Ramonas, L. F. Eastman, J. R. Shealy, and A. Vertiatchikh, Appl. Phys. Lett. **83**, 4038–4040 (2003).
[47]L. Ardaravičius, M. Ramonas, O. Kiprijanovic, J. Liberis, A. Matulionis, L. F. Eastman, J. R. Shealy, X. Chen, and Y. J. Sun, Phys. Status Solidi **202**, 808–811 (2005).
[48]I. Meric, M. Y. Han, A. F. Young, B. Ozyilmaz, P. Kim, and K. L. Shepard, Nat. Nanotechnol. **3**, 654–659 (2008).
[49]K. K. Smithe, C. D. English, S. V. Suryavanshi, and E. Pop, Nano Lett. **18**, 4516–4522 (2018).
[50]X. Chen, C. Chen, A. Levi, L. Houben, B. Deng, S. Yuan, C. Ma, K. Watanabe, T. Taniguchi, D. Naveh, X. Du, and F. Xia, ACS Nano **12**, 5003–5010 (2018).
[51]D. Caughey and R. Thomas, Proc. IEEE **55**, 2192–2193 (1967).
[52]C. Canali, G. Majni, R. Minder, and G. Ottaviani, IEEE Trans. Electron Devices **22**, 1045–1047 (1975).
[53]Z. Zhang, J. Encomendero, R. Chaudhuri, Y. Cho, V. Protasenko, K. Nomoto, K. Lee, M. Toita, H. G. Xing, and D. Jena, Appl. Phys. Lett. **119**, 162104 (2021).
[54]Y. Cho, C. S. Chang, K. Lee, M. Gong, K. Nomoto, M. Toita, L. J. Schowalter, D. A. Muller, D. Jena, and H. G. Xing, Appl. Phys. Lett. **116**, 172106 (2020).
[55]R. Chaudhuri, Z. Chen, D. A. Muller, H. G. Xing, and D. Jena, J. Appl. Phys. **130**, 025703 (2021).

[56]H. Xing, D. S. Green, H. Yu, T. Mates, P. Kozodoy, S. Keller, S. P. DenBaars, and U. K. Mishra, Jpn. J. Appl. Phys. **42**, 50 (2003).
[57]K. Kumakura, T. Makimoto, and N. Kobayashi, Jpn. J. Appl. Phys. **39**, L337 (2000).
[58]J. E. Dill, C. F. C. Chang, D. Jena, and H. G. Xing, J. Appl. Phys. **137**, 025702 (2025).
[59]S. J. Bader, R. Chaudhuri, M. F. Schubert, H. W. Then, H. G. Xing, and D. Jena, Appl. Phys. Lett. **114**, 253501 (2019).
[60]I. Vurgaftman and J. R. Meyer, J. Appl. Phys. **94**, 3675–3696 (2003).
[61]Ł. Janicki, R. Chaudhuri, S. J. Bader, H. G. Xing, D. Jena, and R. Kudrawiec, Phys. Status Solidi – Rapid Res. Lett. **15**, 2000573 (2021).
[62]R. Quay, C. Moglestue, V. Palankovski, and S. Selberherr, Mater. Sci. Semicond. Process. **3**, 149–155 (2000).
[63]J. H. Davies, *The Physics of Low-Dimensional Semiconductors* (Cambridge University Press, 1997).
[64]M. Saraniti and S. Goodnick, IEEE Trans. Electron Devices **47**, 1909–1916 (2000).
[65]J. Leveillee, S. Poncé, N. L. Adamski, C. G. Van de Walle, and F. Giustino, Appl. Phys. Lett. **120**, 202106 (2022).
[66]S. Poncé, D. Jena, and F. Giustino, Phys. Rev. B **100**, 085204 (2019).
[67]T. Kumabe, Y. Ando, H. Watanabe, M. Deki, A. Tanaka, S. Nitta, Y. Honda, and H. Amano, Jpn. J. Appl. Phys. **60**, SBBD03 (2021).